Fusion of CERES, MISR, and MODIS measurements for top-of-atmosphere radiative flux validation

Norman G. Loeb,[1,2] Wenbo Sun,[1] Walter F. Miller,[3] Konstantin Loukachine,[3] and Roger Davies[4,5]

[1] The Clouds and the Earth's Radiant Energy System (CERES), Multiangle Imaging Spectroradiometer (MISR), and Moderate-resolution Imaging Spectroradiometer (MODIS) instruments aboard the Terra satellite make critical measurements of cloud and aerosol properties and their effects on the Earth's radiation budget. In this study, a new multiangle, multichannel data set that combines measurements from all three instruments is created to assess uncertainties in instantaneous shortwave (SW) top-of-atmosphere (TOA) radiative fluxes inferred from CERES Angular Distribution Models (ADMs). MISR Level 1B2 ellipsoid-projected radiances from nine viewing directions in four spectral bands are merged with CERES by convolving the MISR radiances with the CERES Point Spread Function. The merged CERES-MISR data are then combined with the CERES Single Scanner Footprint TOA/Surface Fluxes and Clouds (SSF) product to produce the first merged CERES-MISR-MODIS data set. CERES and MISR data are used to generate narrow-to-broadband regression coefficients to convert narrowband MISR radiances to broadband SW radiances as a function of MODIS-based scene type. The regression uncertainty for all-sky conditions over ocean is approximately 4%. Up to nine SW TOA fluxes for every CERES footprint are estimated by applying the CERES Terra ADMs to each MISR angle. Assuming that differences along the line-of-sight from the different MISR angles are small, the consistency of the TOA fluxes provides an indication of the instantaneous TOA flux uncertainty. The overall relative consistency of all-sky ocean TOA fluxes is 6% (17 W m^{-2}). When stratified by cloud type, TOA fluxes are consistent to 2–3% (<10 W m^{-2}) for moderately thick overcast clouds, which make up 15% of the total population.

1. Introduction

[2] As satellite and surface instrumentation continues to improve with new technological advances, data from a variety of sources are increasingly being merged in order to take full advantage of the complementary nature of the measurements. For quantitative analyses, this requires a thorough understanding of the uncertainties and limitations of parameters retrieved from the measurements. The Earth Observing System Terra satellite (launched in December of 1999) consists of five complementary state-of-the-art instruments offering integrated measurements of the Earth's atmospheric, land, cryospheric and oceanic processes. One of the aims of Terra is to improve the accuracy of estimates of the Earth's radiation budget. To estimate the Earth's radiation budget from satellite measurements, a necessary step involves the conversion of measured radiances to radiative fluxes. New Angular Distribution Models (ADMs) have recently been developed [*Loeb et al.*, 2005] from two years of merged data from the Clouds and the Earth's Radiant Energy System (CERES) [*Wielicki et al.*, 1996] and the Moderate-resolution Imaging Spectroradiometer (MODIS) [*Salomonson et al.*, 1989; *Barnes et al.*, 1998] instruments. The CERES ADMs account for the angular dependence of the radiance field, which is a strong function of the physical and optical characteristics of the scene (e.g., surface type, cloud fraction, cloud/aerosol optical depth, cloud phase, etc.), as well as the illumination angle.

[3] As there is no space-based measurement available that can instantaneously measure radiances in all viewing angles over a scene, there is no direct way of determining the accuracy of ADM-derived TOA fluxes. Instead, the uncertainty must be inferred through a series of consistency tests that approximate the true error. A key requirement of

[1] Center for Atmospheric Sciences, Hampton University, Hampton, Virginia, USA.
[2] Now at NASA Langley Research Center, Hampton, Virginia, USA.
[3] Science Applications International Corporation, San Diego, California, USA.
[4] Jet Propulsion Laboratory, California Institute of Technology, Pasadena, California, USA.
[5] Now at Department of Physics, University of Auckland, Auckland, New Zealand.

this approach is the need for multiangle measurements. Previous studies have shown the value of multiangle measurements for the retrieval and validation of geophysical parameters [*Buriez et al.*, 2001; *Diner et al.*, 2005; *Horváth and Davies*, 2004; *Kahn et al.*, 2001; *Loeb et al.*, 2003b; *Moroney et al.*, 2002; *Parol et al.*, 2004]. *Loeb et al.* [2003b] demonstrated how TOA fluxes inferred from observations in two directions over the same scene provide a useful test of the CERES ADMs. Since TOA flux is by definition independent of satellite viewing geometry, TOA fluxes inferred from multiple directions over the same scene should be identical, provided spatial/temporal matching errors, narrow-to-broadband errors, and parallax effects are negligible. Any difference between the fluxes is an indication of TOA flux uncertainty due to limitations in the ADMs. We note, however, that agreement between fluxes from the different angles is a necessary but insufficient test of the ADMs. That is, even if the fluxes are identical, there is no way of knowing how they compare with the true flux.

[4] In this study, a new merged data set composed of CERES, MODIS and Multiangle Imaging Spectroradiometer (MISR) [*Diner et al.*, 1998, 2002] measurements is created in order to examine the consistency of TOA fluxes from CERES ADMs. In the following, a brief description of the instruments and the merged CERES-MISR-MODIS data set is provided. This is followed by a description of the development of a narrow-to-broadband regression algorithm for converting MISR narrowband radiances to broadband SW values. Finally, CERES ADMs are used to infer SW fluxes from the MISR angles and the consistency of these fluxes is evaluated.

2. Observations

[5] The CERES instrument measures radiances in short-wave ($0.3-5$ μm), window ($8-12$ μm), and total (0.3 to 200 μm) channels at a spatial resolution of approximately ~ 20 km at nadir. It can scan in three modes: cross-track, along-track, and rotating azimuth plane (RAP). CERES scans from limb to limb and provides global coverage each day when in cross-track mode. The MISR instrument provides information on bidirectional reflectance anisotropy and geometric parallax using nine along-track angles from nadir to $70°$ in four visible/near-infrared spectral bands with a spatial resolution of 275 m to 1.1 km. MISR has a 400 km swath width and provides global coverage in $2-9$ days, depending on latitude. The nine cameras of MISR are labeled Df, Cf, Bf, Af, An, Aa, Ba, Ca, and Da, where "f" indicates forward viewing in the along-track direction and "a" aftward viewing. The viewing angles of the D, C, B, and A cameras are $70.4°$, $60.0°$, $45.6°$, and $26.1°$, respectively, and the (An) camera observes nadir. MODIS measures narrowband radiances in 36 spectral bands from the visible to thermal infrared with a spatial resolution from 250 m to 1 km. It has a swath width of 2300 km and provides global coverage every $1-2$ days.

[6] One of the standard data products of CERES is the Single Scanner Footprint TOA/Surface Fluxes and Clouds (SSF) product [*Geier et al.*, 2001; *Loeb et al.*, 2003a]. The SSF product merges CERES parameters including time, position, viewing geometry, radiances and radiative fluxes

with coincident information from MODIS, which is used to characterize the clear and cloudy portions of a CERES footprint. MODIS-SSF parameters include radiances in 5 spectral bands for clear, cloudy and total areas, cloud property retrievals [*Minnis et al.*, 1998, 2003], and aerosol property retrievals from the MOD04 product [*Remer et al.*, 2005], and a second aerosol retrieval algorithm applied to MODIS [*Ignatov and Stowe*, 2002]. Also included in the SSF product are meteorological parameters (e.g., surface wind speed, skin temperature, precipitable water, etc.) from the Global Modeling and Assimilation Office (GMAO)'s Goddard Earth Observing System DAS (GEOS-DAS V4.0.3) product [*Suarez*, 2005].

[7] In this study, the multiangle and multichannel radiances of the MISR Level 1B2 ellipsoid-projected data product are merged with the CERES Terra SSF Edition2B_Rev1 data product by convolving the nine MISR radiances in four spectral bands with the CERES Point Spread Function (PSF) [*Smith*, 1994; *Loeb et al.*, 2003a]. The merged SSF-MISR data set (SSFM) provides a valuable extension to the SSF product as it adds information on the radiance anisotropy of each CERES footprint from nine spatially matched directions in the along-track direction. To create the SSFM data set, all MISR Level 1B2 files from each available orbit in a day are ordered from the NASA Langley Research Center Atmospheric Sciences Data Center (ASDC) and convolved with CERES footprints using a surface reference level. A detailed description of the procedure is provided in Appendix A. A total of sixteen days of the SSFM data product between March 2000 and September 2003 are used in this study. Only days when the CERES instrument is in the along-track scan mode are considered. One full year of SSFM data (for days when CERES is in along-track mode) will soon be available at the ASDC from the following URL: http://asd-www.larc.nasa.gov/ceres/collect_guide/SSF_CG.pdf.

[8] Figures 1a and 1b provide examples of the correlation between CERES, MISR and MODIS radiances for all-sky conditions from the convolution procedure for footprints in which the CERES viewing geometry is within $0.5°$ of the MISR AN camera. In Figure 1a, the correlation coefficient between MISR 0.672 μm and MODIS 0.64 μm radiances is 0.9993 and the relative error in predicted radiances from a least squares fit to the data points is $\approx 3.2\%$. In contrast, the correlation coefficient between CERES SW radiances and MISR radiances (Figure 1b) is 0.9876 and the relative error in the fit is 11%. Clearly, scene-dependent variations in the narrow-to-broadband relationship between MISR and CERES is the reason why the scatter is more pronounced in Figure 1b compared to Figure 1a. As will be shown in the following section, narrow-to-broadband regression errors can be significantly reduced when multichannel regressions as a function of scene type are used.

3. Estimation of SW Radiances From MISR

[9] For a given CERES footprint, conversion of narrowband MISR radiances at each of the nine MISR angles to broadband SW radiances is determined by applying empirical narrow-to-broadband regression relations that relate MISR radiances in the blue (440 nm), red (672 nm) and
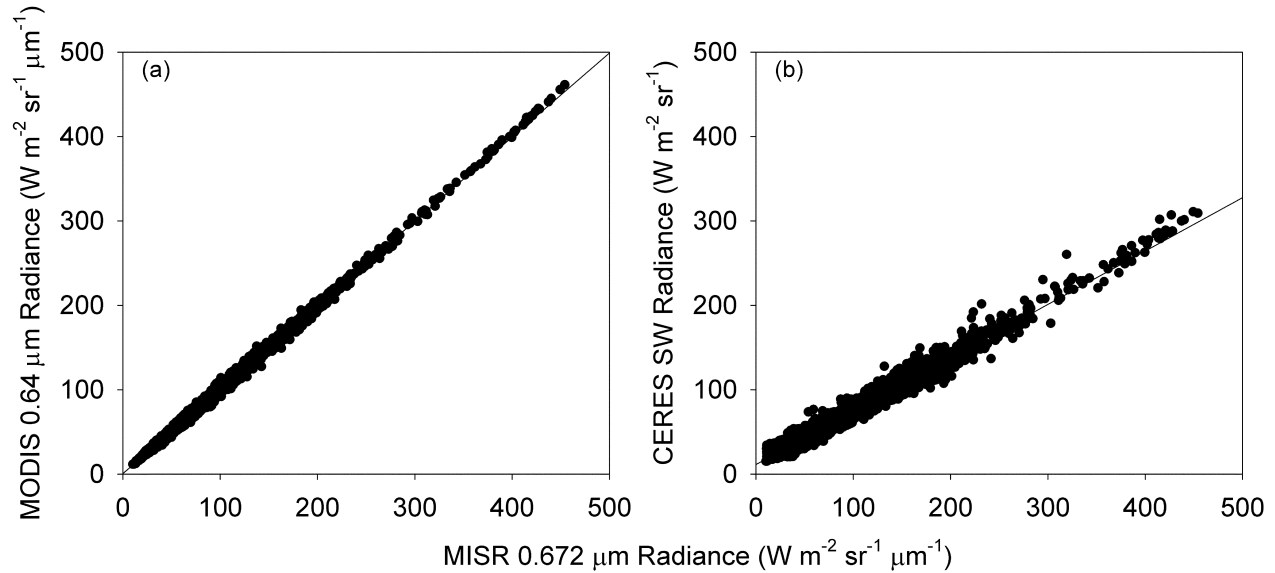
Figure 1. (a) MODIS and MISR nadir radiances in the red band averaged over CERES footprints for all-sky conditions on 12 September 2000. Only footprints in which the CERES viewing geometry lies within 0.5° of the MISR AN camera are shown. (b) CERES SW and MISR red channel radiances for the same footprints as in Figure 1a. Solid line is the regression fit.
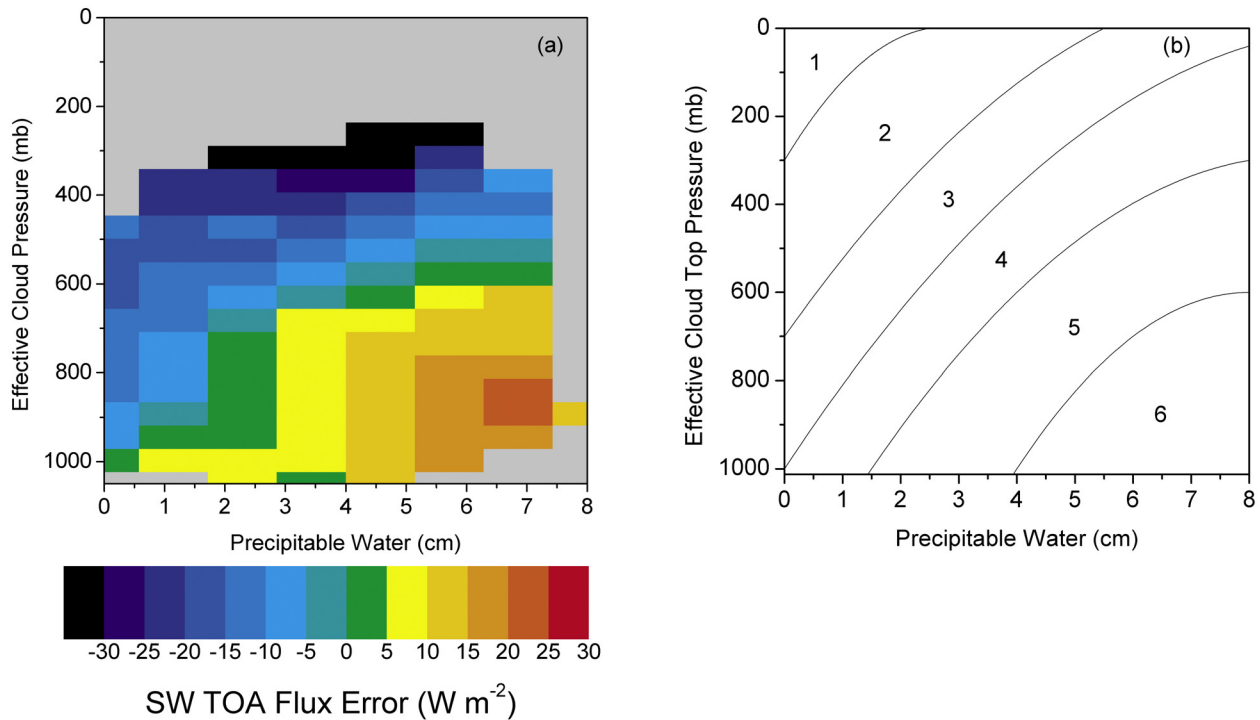

Figure 2. (a) Error in instantaneous SW TOA flux for tropical ocean overcast liquid water clouds inferred from the errors in radiances estimated from a narrow-to-broadband regression analysis that does not explicitly account for effective pressure and precipitable water variations. CERES anisotropic factors are used to convert from a radiance error to a flux error. (b) Empirically derived contours defining effective pressure and precipitable water domains in Figure 2a.

Table 1. Coefficients of Second-Order Polynomials Defining the P and W Stratification of Narrow-to-Broadband Regressions Used in This Study

Curve	a_0	a_1	a_2
1	300.000	−220.000	40.000
2	700.000	−187.272	10.910
3	1000.000	−200.000	10.000
4	1318.462	−231.924	13.076
5	2200.000	−400.000	25.000

near-infrared (867 nm) bands with a SW radiance estimate ($\hat{I}_{sw}$) as follows:

$$\hat{I}_{sw} = c_o + c_1 I_{blue} + c_2 I_{red} + c_3 I_{nir} \qquad (1)$$

where I_{blue} I_{red}, and I_{nir} denote the MISR blue, red, and near-infrared radiances, respectively, and c_o, c_1, c_2 and c_3 correspond to regression coefficients. Information from the green band was typically redundant with that from the red band, so it was not used. The regression coefficients are derived from coincident CERES SW and MISR narrow-band radiances from sixteen days of merged CERES-MISR-MODIS global data. Separate regression fits are derived for predefined intervals of solar zenith angle, viewing zenith angle, relative viewing azimuth angle, cloud fraction, effective cloud top pressure, precipitable water, and surface scene type. The solar zenith and viewing zenith angle intervals are 10° wide, while 20°-wide intervals are used to stratify in relative viewing azimuth angle. Cloud fraction is divided into 11 classes: clear, and ten bins from 0% to 100% in increments of 10%. The effective cloud top pressure (P) and precipitable water (W) intervals are determined empirically by analyzing the distribution of radiance errors obtained when narrow-to-broadband regressions that are not explicit functions of P and W are applied. Figure 2a shows an example for overcast clouds over tropical oceans. For the average condition in which the narrow-to-broadband regression coefficients were derived, water vapor absorption above the clouds is underestimated for moist low cloud conditions and radiances are overestimated by the regression (positive residuals in Figure 2a). Conversely, for high clouds and in regions of low precipitable water, water vapor absorption above the clouds is overestimated and radiances are underestimated (negative residuals in Figure 2a). In terms of instantaneous SW TOA flux, the range in the error exceeds 60 W m^{-2}. In order to develop narrow-to-broadband regression relations that explicitly account for P and W variations, empirical fits that approximate the two-dimensional shape of TOA flux errors in Figure 2a are used. Six P–W domains are defined using a second-order polynomial fit given by:

$$P = a_0 + a_1 W + a_2 W^2 \qquad (2)$$

[10] The coefficients of each curve are provided in Table 1, and the curves are illustrated in Figure 2b.

[11] To assess the uncertainty in the narrow-to-broadband regressions, the regressions are applied to one day of global

data that was not used in deriving the regression coefficients. Only footprints in which the CERES viewing zenith and relative azimuth angles lie within 2° of a MISR camera are considered to test the regression models. Since the narrow-to-broadband regression is only a weak function of viewing zenith angle, a 2° difference between MISR and CERES has a negligible effect. The overall relative bias and relative root-mean-square (RMS) error of the narrowband-to-broadband radiance conversion is −0.25% and 3.83%, respectively. Also, no dependence on P or W are found for all cloud types. When only clear and overcast footprints are considered, the relative RMS error in the narrow-to-broadband regression is ≈3%. For footprints that consist of a mix of cloudy and clear areas, the relative RMS error is ≈6%.

[12] Uncertainties in the narrow-to-broadband regressions from this study are significantly smaller than those from previous studies. For example, *Li and Leighton* [1992] derived regression relations between Advanced Very High Resolution Radiometer (AVHRR) narrowband and Earth Radiation Budget Experiment (ERBE) broadband SW reflectances and obtained a relative RMS error of 7% in all-sky conditions. Similar narrow-to-broadband accuracies were obtained by *Li and Trishchenko* [1999] using visible and shortwave albedos from the Scanner for Radiation Budget (ScaRaB) instrument.

4. SW TOA Flux Consistency

[13] After applying the narrow-to-broadband regressions to estimate SW radiances from each of the nine MISR cameras, the next step is to infer SW TOA fluxes from each MISR angle. A SW TOA flux is determined from the following:

$$\hat{F}_{sw}(\theta_o, \theta_j, \phi_j) = \frac{\pi \hat{I}_{sw}(\theta_o, \theta_j, \phi_j)}{R(\theta_o, \theta_j, \phi_j)} \qquad (3)$$

where $\hat{I}_{sw}(\theta_o, \theta_j, \phi_j)$ is the SW radiance estimated from MISR radiances in camera j, $R(\theta_o, \theta_j, \phi_j)$ is the CERES SW anisotropic factor [*Loeb et al.*, 2005] corresponding to the scene as inferred from MODIS measurements, and $(\theta_o, \theta_j, \phi_j)$ corresponds to the solar zenith angle, viewing zenith angle and relative azimuth angle of the jth camera. For a given CERES footprint, a measure of the consistency in the ADM-derived TOA fluxes from MISR "broadband" SW radiances is given by the sample standard deviation of the flux estimates:

$$s_i = \sqrt{\frac{\sum_{j=1}^{n} \left(\hat{F}_{ij}^{sw} - \langle \hat{F}_i^{sw} \rangle \right)^2}{n-1}} \qquad (4)$$

where $\langle \hat{F}_i^{sw} \rangle$ is the average estimated SW TOA flux for the ith CERES footprint from n MISR angles. Only footprints with $n \geq 5$ are considered in the analysis. For clear scenes, MISR viewing angles that lie within 15° of the specular direction are omitted from the analysis. No such constraints
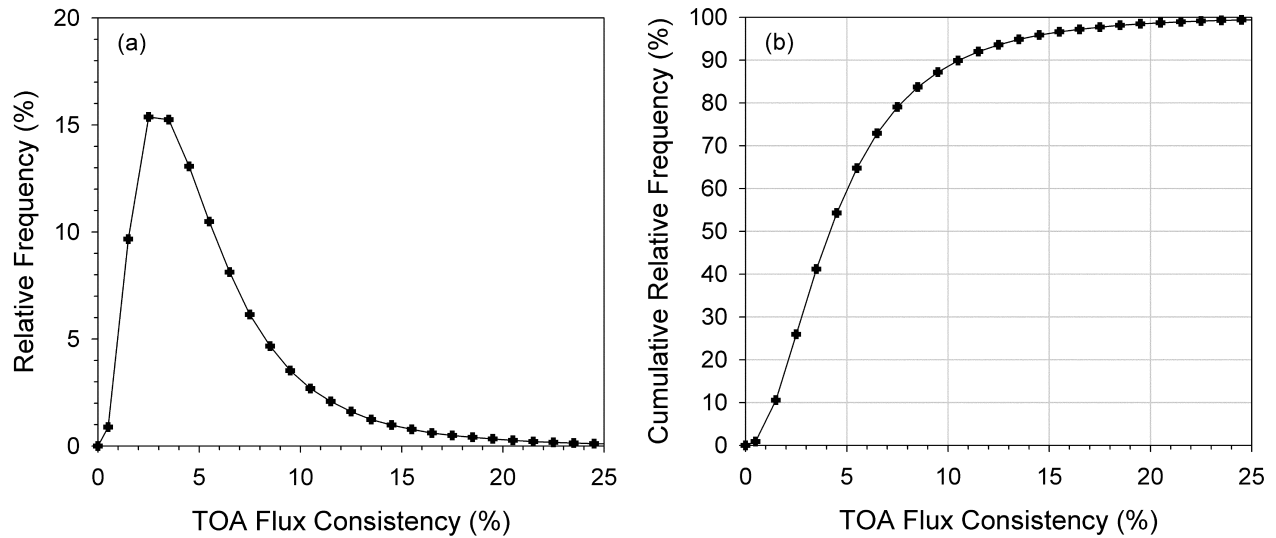
Figure 3. (a) Relative frequency and (b) cumulative relative frequency of SW TOA flux consistency for global all-sky conditions over ice-free ocean.

on sunglint are used if the cloud fraction within a CERES footprint exceeds 0.1%. The relative TOA flux consistency is determined by the coefficient of variation, which is given by:

$$CV_i = \frac{s_i}{\langle \hat{F}_i^{sw} \rangle} \times 100\% \qquad (5)$$

[14] Since the analysis uses only days when the CERES instrument is in the along-track scan mode, the merged CERES, MISR and MODIS measurements are always located relatively close to the Terra ground track. As a result, the scene identification from MODIS that is used to select CERES anisotropic factors at the MISR angles is close to nadir. Therefore results from this approach are only really representative of conditions when CERES scans in the along-track direction. If it were possible to determine the instantaneous TOA flux consistency when CERES scans in the cross-track direction, the results could be quite different for two reasons: (1) The relative azimuth angles sampled would differ by 90° from the along-track direction and (2) cloud retrieval dependencies on viewing geometry could influence the selection of anisotropic factors at different view angles. A necessary (but not sufficient) test of the latter effect is obtained by examining the viewing zenith angle dependence of mean CERES TOA fluxes. *Loeb et al.* [2006a] examined this and found that for all-sky conditions the viewing zenith angle dependence in mean SW TOA fluxes is <2%.

[15] Figures 3a–3b show the relative frequency and cumulative frequency distributions of CV_i for all CERES footprints over ice-free ocean. The mode of the distribution in Figure 3a lies between 2% and 3%. Approximately 55% of the footprints have a relative TOA flux consistency of <5%, and more than 98% of the footprints have $CV_i < 20\%$. In a similar study, L. Di Girolamo et al. (personal communication, 2005) compare the consistency

of cloud optical depth retrievals for liquid water clouds by applying a version of the MODIS cloud retrieval algorithm [*Platnick et al.*, 2003] to infer cloud optical depths from each MISR angle. That study finds that 70% to 80% of the MODIS retrieved cloud optical depths for water clouds have relative TOA flux consistencies of less than 20%.

[16] For a population of M CERES footprints, the overall relative consistency of the SW TOA fluxes is determined from:

$$\overline{CV} = \left(\frac{\sqrt{\frac{1}{M}\sum_{i=1}^{M} s_i^2}}{\frac{1}{M}\sum_{i=1}^{M} \langle \hat{F}_i^{sw} \rangle} \right) \times 100\% \qquad (6)$$

[17] The relative consistency of the SW TOA fluxes for a given scene type depends upon how well the CERES SW ADMs represent the anisotropy of a scene and on the accuracy in the narrow-to-broadband regression. An estimate of the latter error is determined by comparing CERES SW radiances with predicted MISR SW radiances when CERES observes a scene from the same viewing geometry as one of the nine MISR cameras. Here, only footprints in which the CERES viewing zenith and relative azimuth angles are within 2° of the corresponding angles for one of the MISR cameras are used to evaluate the narrow-to-broadband error. The narrow-to-broadband regression error is removed from the total error (CV_T) as follows:

$$CV_{ADM} = \sqrt{CV_T^2 - CV_{NB}^2} \qquad (7)$$

where CV_{NB} is the relative error in the narrow-to-broadband regression for a given cloud type.
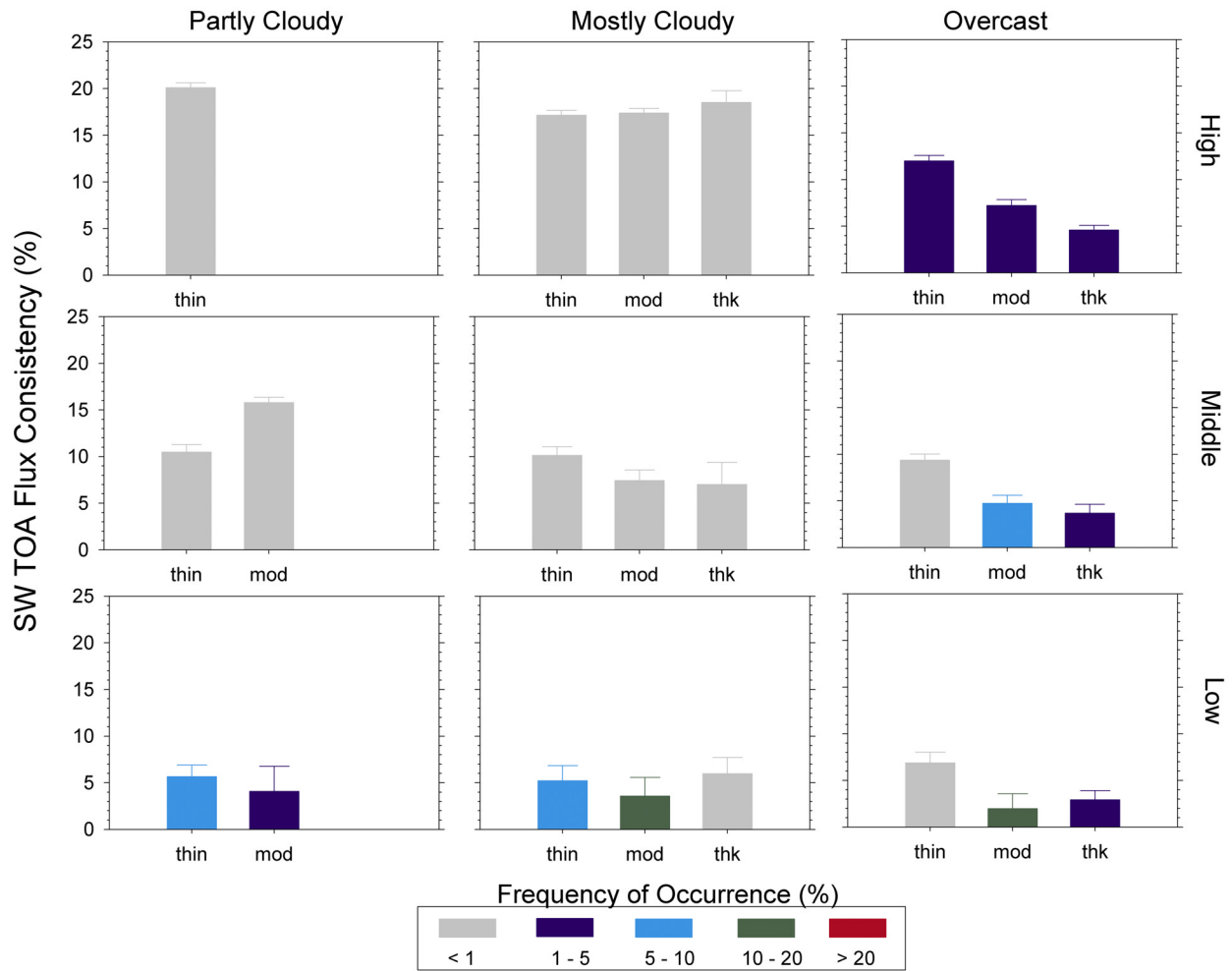
Figure 4. SW TOA flux consistency over ocean for single-layer clouds defined in Table 2. Colors represent the frequency of occurrence of each cloud type.

[18] Figure 4 shows the SW TOA flux consistency of single-layer clouds for the cloud types defined in Table 2. Clouds within a CERES footprint are classified as single-layer when only one of the three height classes (low, middle or high) is present. Error bars in Figure 4 provide the uncertainty in the TOA flux consistency due to narrow-to-broadband regression errors. The lower bound of the error bars corresponds to the relative consistency after removing the narrow-to-broadband regression error from the total (equation (7)), while the upper bound of the error bars includes narrow-to-broadband regression errors. No attempt is made to account for errors caused by scene differences between the various MISR viewing directions. Since a surface reference level is used to collocate MISR pixels from different viewing directions over a CERES footprint, the scene along the line-of-sight of the MISR angles can be different, particularly for high and/or inhomogeneous clouds.

[19] In spite of this, the relative consistency remains within 6% (17 W m^{-2}) overall. The relative consistency for single-layer low-level clouds remains within 7%, and is as low as 2–3% (<10 W m^{-2}) for moderately thick overcast clouds. These clouds are the most frequently occurring cloud type, making up approximately 15% of the total

population (i.e., including clear, single-layer and multilayer clouds). TOA fluxes for partly and mostly cloudy high clouds (cloud types 19 through 24) show more scatter than the lower clouds. The TOA flux consistency is generally 15–20%, but their combined frequency of occurrence is less than 0.75% of the total population. High overcast clouds

Table 2. Scene Type Classification Scheme Used in Multiangle TOA Flux Consistency Tests[a]

	PCL			MCL			OVC		
	Thin	Moderate	Thick	Thin	Moderate	Thick	Thin	Moderate	Thick
High	19	20	21	22	23	24	25	26	27
Middle	10	11	12	13	14	15	16	17	18
Low	1	2	3	4	5	6	7	8	9

[a]Each CERES footprint is assigned a scene identification index from 1 through 27 based on the cloud fraction (f), mean effective cloud top pressure (p_t), cloud optical depth ($e^{\langle \ln \tau \rangle}$). For clear cases, $f \leq 0.001$; for PCL cases, $0.001 < f \leq 0.4$; for MCL cases, $0.4 < f \leq 0.99$; and for OVC cases, $0.99 < f \leq 1.0$. For high cases, $p_t < 440$ mb; for middle cases, 440 mb $\leq p_t < 680$ mb; and for low cases, $p_t \geq 680$ mb. For thin cases, $e^{\langle \ln \tau \rangle} \leq 3.35$; for moderate cases $3.35 < e^{\langle \ln \tau \rangle} \leq 22.63$; and for thick cases, $e^{\langle \ln \tau \rangle} > 22.63$.
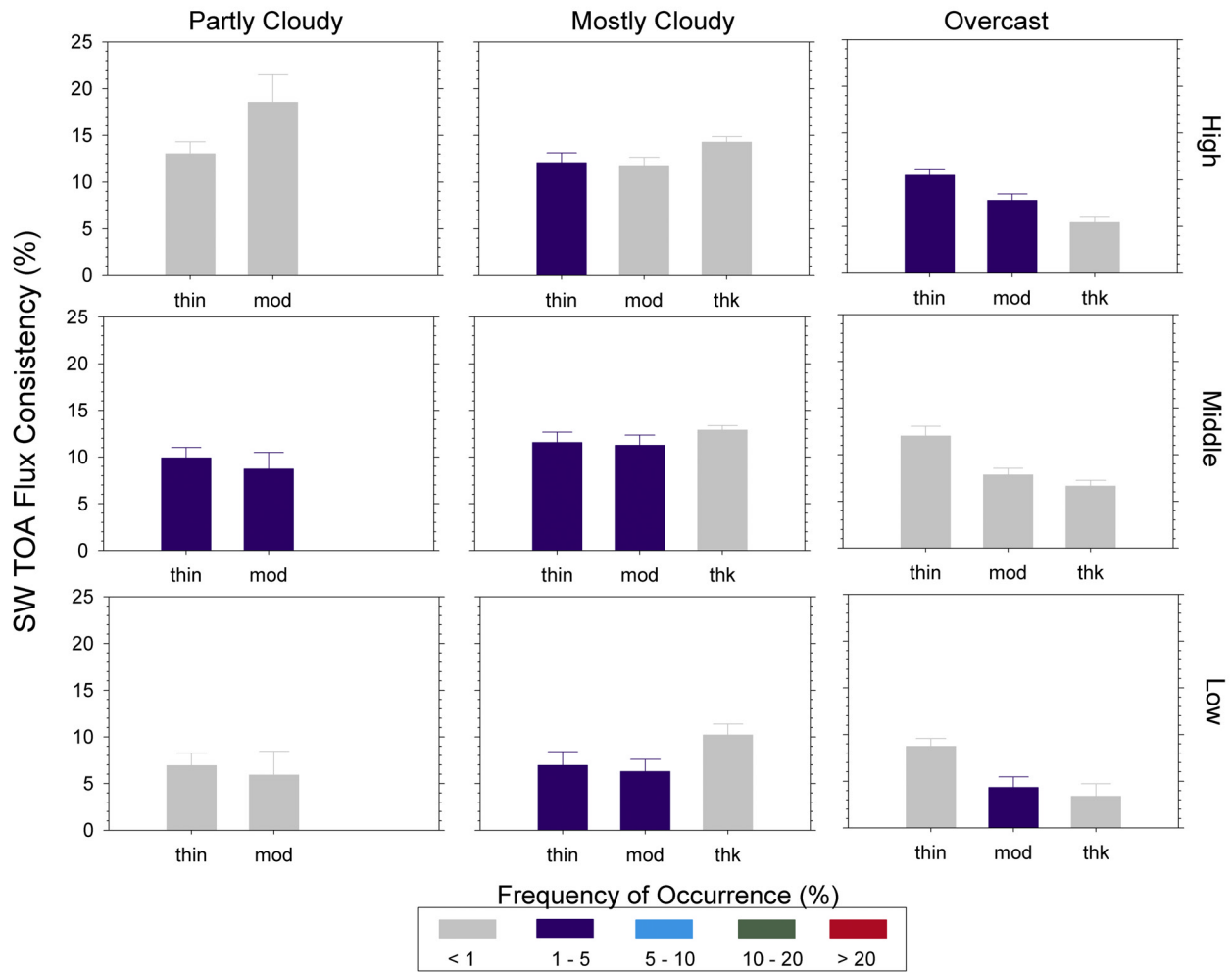
Figure 5. Same as in Figure 4 but for multilayer clouds.

occur approximately 9% of the time, and the TOA flux consistency ranges from 4% for thick clouds to 12% for thin clouds. Note that in units of W m^{-2}, the range in TOA flux consistency for high overcast clouds is much smaller, lying between 25 W m^{-2} and 30 W m^{-2}.

[20] Multilayer clouds occur when clouds within a CERES footprint lie in more than one of the cloud effective pressure intervals in Table 2. Overall, approximately 32% of the CERES footprints fall in this category. The TOA flux consistency for multilayer clouds is approximately 8.5% (21 W m^{-2}), compared to 5% (15 W m^{-2}) for single-layer clouds. Figure 5 shows the SW TOA flux consistency of multilayer clouds for the cloud types defined in Table 2. Multilayer clouds classified by using area-weighted averages of cloud effective pressure and logarithm of cloud optical depth. Therefore, if a CERES footprint contains both low and high cloud layers, the footprint will be classified as low (high) if most of the cloud area coverage is in the low (high) effective cloud top pressure interval range. For multilayer clouds falling in the low cloud category, the TOA flux consistency is approximately 5.8% (14 W m^{-2}). By comparison, the TOA flux consistency for middle-level and high-level clouds is 11% (22 W m^{-2}) and 9.5% (29 W m^{-2}), respectively.

[21] For clear ocean scenes, only MISR angles that are $\geq 15°$ away from the specular reflection direction are considered. This constraint, together with the requirement of at least 5 MISR angles per CERES footprint ($n \geq 5$ in equation (4)), results in a sample size that is only 1.9% of the total population. For these footprints, the TOA flux consistency is approximately 4.9% (4.3 W m^{-2}). If a glint angle cutoff of 25° is used, the TOA flux consistency decreases to 3.3% (3 W m^{-2}), but the number of clear ocean samples decreases by approximately 40%.

5. SW TOA Flux Relative Bias by Viewing Zenith Angle

[22] Results thus far have focused on estimates of the consistency in instantaneous TOA fluxes from CERES ADMs without any indication of whether systematic biases in the mean TOA flux with viewing zenith angle exist. In an earlier study, *Suttles et al.* [1992] found a rather large 10% increase in all-sky SW TOA flux with viewing zenith angle from ERBE ADMs. More recently, *Loeb et al.* [2006a] showed that such biases are absent when all-sky CERES TOA fluxes based on the new CERES Terra ADMs are considered. Here, we extend that analysis by focusing on
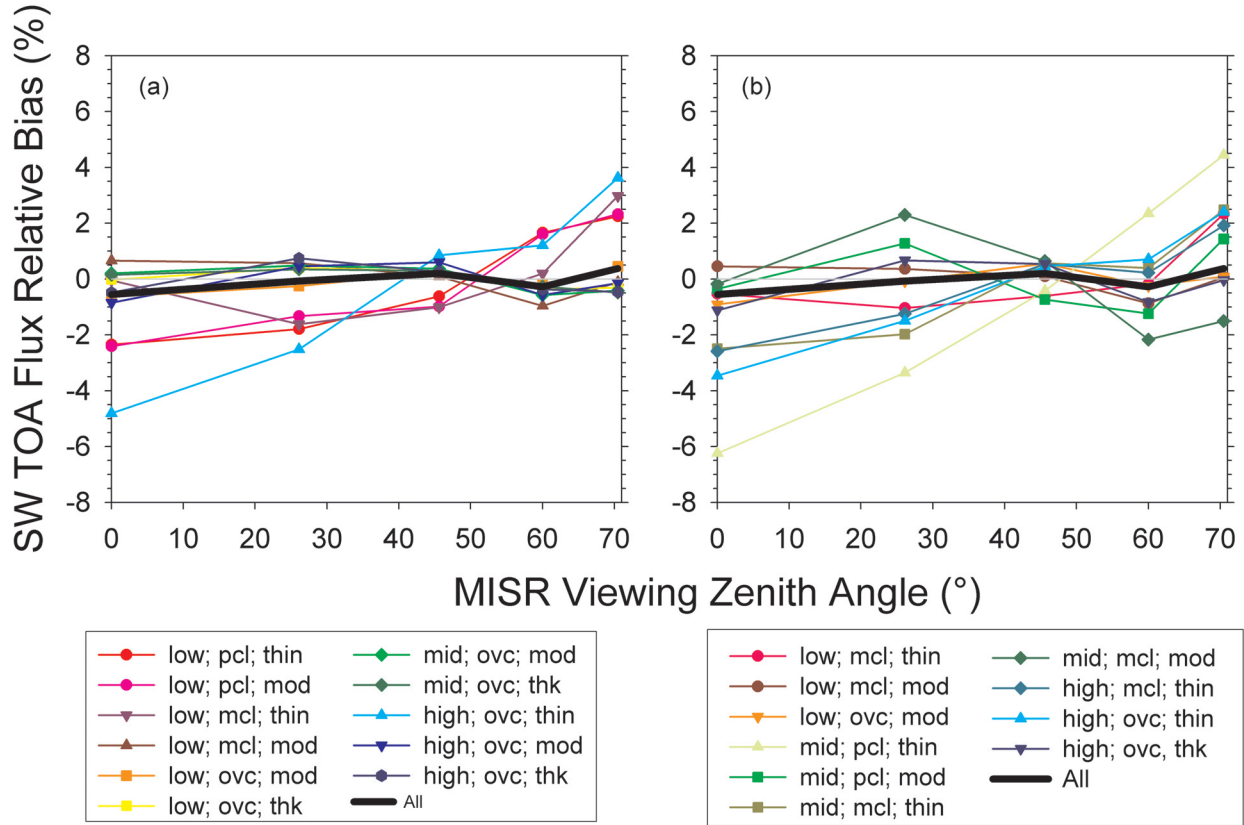
Figure 6. SW TOA flux relative bias against MISR viewing zenith angle by cloud type for (a) single-layer clouds and (b) multilevel clouds. The solid black line in each plot corresponds to the all-sky case (single+multilayer).

the viewing zenith angle dependence of mean TOA fluxes by cloud type using the SSFM data. For each cloud type considered in Table 2 with a frequency-of-occurrence >1%, the following metric is used to quantify the relative bias in TOA flux with viewing zenith angle:

$$\bar{\delta}_j = \frac{\sum_{i=1}^{M} \left(\hat{F}_{ij}^{sw} - \langle \hat{F}_i^{sw} \rangle \right)}{\sum_{i=1}^{M} \langle \hat{F}_i^{sw} \rangle} \times 100\% \qquad (8)$$

[23] $\bar{\delta}_j$ is evaluated at five distinct viewing zenith angles (0.0°, 26.1°, 45.6°, 60.0°, 70.4°) corresponding to fore and aft MISR camera directions (i.e., An, Af/Aa, Bf/Ba, Cf/Ca, Df/Da). Figures 6a and 6b provide SW TOA flux relative biases against viewing zenith angle and cloud type for single-layer and multilevel clouds, respectively. The overall relative bias (indicated by the thick black line) remains <0.5% at all angles, consistent with *Loeb et al.* [2006a]. For single-layer clouds, $\bar{\delta}_j$ is generally <1% for all cloud types except partly cloudy low, mostly cloudy thin and overcast high thin cloud types. The largest relative biases for multilevel clouds occur for thin clouds with average effective pressure falling in the middle and high cloud height classes. For the partly cloudy middle thin, overcast high thin and mostly cloud high thin classes, TOA fluxes increase

with viewing zenith angle. While these larger relative uncertainties in SW TOA flux will strongly influence daily mean regional fluxes, the monthly mean biases will be much smaller because a given region is sampled from a range of viewing zenith angles during the course of a month [*Loeb et al.*, 2003b]. As a result, the errors partially cancel in the monthly mean. This is confirmed by *Loeb et al.* [2006a] who show that regional RMS errors in SW TOA flux range from only 0.75 to 1.6 W m^{-2} (24-h average).

6. Summary and Conclusions

[24] In this study, a new data set that merges CERES, MISR and MODIS is created in order to evaluate instantaneous SW TOA fluxes on the basis of CERES Angular Distribution Models (ADMs). For every CERES footprint, radiances from nine MISR angles in four spectral bands are convolved with the CERES Point Spread Function (PSF) to provide spatially matched MISR and CERES measurements. When these data are combined with data in the CERES Single Scanner Footprint TOA/Surface Fluxes and Clouds (SSF) product, each CERES footprint effectively contains multiangle, multispectral and broadband radiances, in addition to cloud and aerosol property retrievals based on MODIS measurements, and meteorological parameters from the GEOS-DAS V4.0.3 product.

[25] To convert the spectral MISR radiances in each angle to a SW radiance, a narrow-to-broadband regression analysis is performed using CERES SW and MISR narrowband radiances. Narrow-to-broadband coefficients from this analysis are produced as a function of viewing geometry, MODIS-derived cloud fraction and effective pressure, and GEOS-DAS V4.0.3 precipitable water. For all-sky ocean, the instantaneous uncertainty in SW radiance from the regression is approximately 4%.

[26] TOA flux consistency is determined by comparing ADM-derived TOA fluxes inferred from every MISR angle over a CERES footprint. Assuming that differences along the line-of-sight from the different MISR angles are small, the consistency of the TOA fluxes provides an estimate of the instantaneous SW TOA flux uncertainty from CERES ADMs. Sixteen days of merged CERES-MISR-MODIS data when CERES is in along-track mode are considered. The overall consistency of CERES ADM-derived TOA fluxes for all-sky ocean is 6% (17 W m^{-2}). Approximately 55% of the footprints have a relative TOA flux consistency of <5%, and more than 98% of the footprints have a TOA flux consistency of <20%. TOA fluxes for low-level moderately thick overcast clouds, the most dominant cloud type, present 15% of the time, are consistent to within 2–3% (<10 W m^{-2}). For high overcast clouds, the TOA flux consistency ranges from 4% for thick clouds to 12% for thin clouds. Results are generally worse for partly and mostly cloudy high clouds, but these represent a small fraction of the total cloud population. TOA flux consistency is generally better for single-layer than for multilayer clouds. For cloud-free ocean, TOA fluxes are generally consistent to 3–5% (3–4.5 W m^{-2}), depending on how sunglint is screened in the analysis. Furthermore, for most cloud types SW TOA fluxes from CERES ADMs show no systematic bias with viewing zenith angle. The exception occurs for broken thin and overcast high thin clouds, where SW fluxes increase with viewing zenith angle.

[27] In this study, no attempt was made to account for errors caused by parallax which occurs because a surface reference level is used to collocate MISR observations from different viewing directions. For high and/or inhomogeneous clouds, the scene at cloud level observed from two MISR directions can be quite dissimilar because they see different portions of the cloud. For example, if the cloud height is 10 km and the viewing zenith angle separation is 55°, the separation distance at cloud level is as large as 14 km. Therefore, for high-level clouds, a large fraction of RMS difference between fluxes from the different MISR angles is likely due to the parallax effect.

[28] The new merged CERES-MISR-MODIS data set introduced in this study can be useful for several other applications besides CERES TOA flux validation. Because the measurements from the three instruments are so well matched spatially, the data are ideal for monitoring the relative calibration stability of CERES, MISR, and MODIS with time. Preliminary results indicate that during the first five years of the Terra mission, the calibration of these instruments remained stable to <1% relative to one another [*Loeb et al.*, 2006b]. Since MISR produces a TOA albedo product at visible wavelengths (called the ''MISR Level 2 Top of Atmosphere/Cloud Albedo Product'' [*Diner et al.*, 1999]), the narrow-to-broadband regressions developed in

this study can also be adapted to convert visible MISR albedos to broadband SW albedos. SW MISR albedos can then be directly compared with albedos derived from CERES. The combined CERES, MISR, and MODIS data can also be used to understand the conditions under which the MISR and CERES albedos agree or disagree (e.g., by cloud type), how the TOA flux consistency of CERES TOA fluxes behave under these conditions, and what the degree of anisotropy is. Clearly, merging complementary data such as CERES, MISR, and MODIS opens a new window of opportunity for discovery that cannot be realized if data from each instrument are analyzed independently.

Appendix A: Merging of MISR and SSF Product

[29] The MISR instrument provides radiometrically and geometrically calibrated images in four spectral bands at nine angles. The MISR Level 1B2 product includes the ellipsoid-projected georectified radiance product (GRP), which provides TOA radiances projected on the WGS84 reference ellipsoid. The solar and viewing geometries at which the radiances in the GRP files are measured are stored in the MISR Geometric Parameter (GP) files. Geolocation data on a Space Oblique Mercator (SOM) grid are given in the MISR Ancillary Geographic Product (AGP). The Terra satellite orbits the Earth approximately 15 times each day and has a total of 233 distinct orbits that are repeated every 16 days. These 233 repeating orbits are called paths. Each path is divided into 180 blocks measuring 563.2 km (cross-track) × 140.8 km (along-track). For a given path, a numbered block always contains the same geographic locations. Because of seasonal variations in the portion of the Earth that is in daylight, only up to about 142 blocks contain valid data at any given time. There are a total of 233 AGP files, one for each of the 233 paths of Terra.

[30] The MISR L1B2 GRP, GP, and AGP files are stored in EOS-HDF format. Only MISR data from Collections 5 and 6 are considered. To merge the MISR measurements and the CERES SSF data set, the radiance data in the MISR L1B2 GRP, solar and viewing angle data in the GP, and latitude and longitude in the AGP files are first extracted from the archive and stored in temporary files in binary format. These temporary files are then read simultaneously and the observation time, radiances, solar and viewing angles, and geolocation of each MISR pixel are matched following the measurement pixel order and stored in a combined MISR binary file. The observation time, provided only for blocks in the MISR GRP files, is then interpolated to individual pixels, as required by the CERES convolution (below). Next, all of the radiances and solar and viewing angles are interpolated to a common spatial grid. The latitude and longitude in the MISR AGP have a spatial resolution of 1100 m, the spatial resolution of the solar and viewing angles in the MISR GP is 17,600 m, and radiances in the MISR L1B2 GRP have spatial resolutions of 275 m for the 672 nm channel of all cameras, 275 m for all channels of the Nadir (AN) camera, and 1100 m for the remaining cameras and channels. A 1100 m × 1100 m geolocation grid is used to collocate the measurements. The accuracy of the MISR Level 1B2 radiance is provide by the Radiometric Data Quality Indicator (RDQI), saved

as the first two digits of the Radiance/RQDI data in the MISR L1B2 GRP. The RDQI is an integer in the range of 0 to 3. Only the radiances with the highest radiometric accuracy (i.e., RDQI = 0) are used in the convolution with the CERES SSF data.

[31] The combined MISR binary files are the inputs to the CERES convolution algorithm [*Green and Wielicki*, 1996] which averages the MISR pixel-level radiances into CERES-footprint-level data. To achieve the closest spatial match between the CERES and MISR, the distribution of energy received at the CERES broadband detectors must be taken into account when averaging the MISR measurements or MODIS-derived properties over the CERES footprint. This distribution of energy is described by the CERES PSF. The PSF accounts for the effects of detector response, optical field-of-view (FOV), and electronic filters [*Smith*, 1994]. To determine appropriately weighted and matched MISR radiances over CERES FOVs, pixel-level MISR data from the MISR L1B2 ellipsoid-projected orbital GRP files are used. A grid that covers the SSF footprint at the MISR pixel angular resolution is created with weights defined by:

$$w(\delta, \beta) = \iint\limits_{Footprint} P(\delta, \beta) \cos \delta d\delta d\beta \qquad (A1)$$

where $P(\delta, \beta)$ is the CERES PSF, and δ and β are the angular coordinates of a point within a CERES footprint [*Green and Wielicki*, 1996]. The radiances that are assigned to a grid square are geometrically averaged and then weighted by the PSF for that grid square. The footprint average is then obtained from:

$$\langle I \rangle = \frac{\iint\limits_{Footprint} P(\delta, \beta) I(\delta, \beta) \cos \delta d\delta d\beta}{\iint\limits_{Footprint} P(\delta, \beta) \cos \delta d\delta d\beta}, \qquad (A2)$$

where $I(\delta, \beta)$ is the MISR pixel-level radiance, This process produces the SSFM data product composed of hourly MISR radiance statistics over CERES footprints. The time delay between the MISR camera views is $40-55$ s, resulting in a total time span of approximately 7 min between DF and DA for each scene.

[32] Footprints in the SSFM data set are stored in the order as footprints in the CERES SSF product. By simultaneously reading data from this file and the SSF product, all merged CERES-MISR-MODIS parameters are available for data analysis.

References

Barnes, W. L., T. S. Pagano, and V. V. Salomonson (1998), Prelaunch characteristics of the Moderate Resolution Imaging Spectroradiometer (MODIS) on EOS-AM1, *IEEE Trans. Geosci. Remote Sens.*, *36*, 1088–1100.

Buriez, J.-C., M. Doutriaux-Boucher, F. Parol, and N. G. Loeb (2001), Angular variability of the liquid water cloud optical thickness retrieved from ADEOS-POLDER, *J. Atmos. Sci.*, *58*(20), 3007–3018.

Diner, D. J., et al. (1998), Multiangle Imaging SpectroRadiometer (MISR) description and experiment overview, *IEEE Trans. Geosci. Remote Sens.*, *36*, 1072–1087.

Diner, D. J., R. Davies, T. Varnai, C. Moroney, C. Borel, S. A. W. Gerstl, and D. L. Nelson (1999), Level 2 Top-of-Atmosphere Albedo, Multi-Angle Imaging Spectroradiometer Algorithm Theoretical Basis Document, NASA Goddard Space Flight Cent., Greenbelt, Md. (Available at http://eospso.gsfc.nasa.gov/eos_homepage/for_scientists/atbd/viewInstrument.php?instrument = 9)

Diner, D. J., J. C. Beckert, G. W. Bothwell, and J. I. Rodriguez (2002), Performance of the MISR instrument during its first 20 months in Earth orbit, *IEEE Trans. Geosci. Remote Sens.*, *40*(7), 1449–1466.

Diner, D. J., et al. (2005), The value of multiangle measurements for retrieving structurally and radiatively consistent properties of clouds, aerosols, and surfaces, *Remote Sens. Environ.*, *97*, 495–518.

Geier, E. B., R. N. Green, D. P. Kratz, P. Minnis, W. F. Miller, S. K. Nolan, and C. B. Franklin (2001), Single satellite footprint TOA/surface fluxes and clouds (SSF) collection document, NASA Langley Res. Cent., Hampton, Va. (Available at http://asd-www.larc.nasa.gov/ceres/collect_guide/SSF_CG.pdf)

Green, R. N., and B. A. Wielicki (1996), Convolution of imager cloud properties with CERES footprint point spread function (Subsystem 4. 4), Clouds and the Earth's Radiant Energy System (CERES) Algorithm Theoretical Basis Document, NASA Langley Res. Cent., Hampton, Va. (Available at http://asd-www.larc.nasa.gov/ATBD/ATBD.html)

Horváth, Á., and R. Davies (2004), Anisotropy of water cloud reflectance: A comparison of measurements and 1D theory, *Geophys. Res. Lett.*, *31*, L01102, doi:10.1029/2003GL018386.

Ignatov, A., and L. L. Stowe (2002), Aerosol retrievals from individual AVHRR channels: I. Retrieval algorithm and transition from Dave to 6S radiative transfer model, *J. Atmos. Sci.*, *59*, 313–334.

Kahn, R., P. Banerjee, and D. McDonald (2001), The sensitivity of multiangle imaging to natural mixtures of aerosols over ocean, *J. Geophys. Res.*, *106*, 18,219–18,238.

Li, Z., and H. G. Leighton (1992), Narrowband to broadband conversion with spatially autocorrelated reflectance measurements, *J. Appl. Meteorol.*, *31*, 421–432.

Li, Z., and A. Trishchenko (1999), A study toward an improved understanding of the relationship between visible and shortwave measurements, *J. Atmos. Oceanic Technol.*, *16*, 347–360.

Loeb, N. G., S. Kato, N. Manalo-Smith, S. K. Gupta, W. F. Miller, P. Minnis, and B. A. Wielicki (2003a), Angular distribution models for top-of-atmosphere radiative flux estimation from the Clouds and the Earth's Radiant Energy System instrument on the Tropical Rainfall Measuring Mission satellite. Part I: Methodology, *J. Appl. Meteorol.*, *42*, 240–265.

Loeb, N. G., K. Loukachine, N. Manalo-Smith, B. A. Wielicki, and D. F. Young (2003b), Angular distribution models for top-of-atmosphere radiative flux estimation from the Clouds and the Earth's Radiant Energy System instrument on the Tropical Rainfall Measuring Mission satellite. Part II: Validation, *J. Appl. Meteorol.*, *42*, 1748–1769.

Loeb, N. G., S. Kato, K. Loukachine, and N. Manalo-Smith (2005), Angular distribution models for top-of-atmosphere radiative flux estimation from the Clouds and the Earth's Radiant Energy System instrument on the *Terra* satellite. Part I: Methodology, *J. Atmos. Oceanic Technol.*, *22*, 338–351.

Loeb, N. G., S. Kato, K. Loukachine, and N. Manalo-Smith (2006a), Angular distribution models for top-of-atmosphere radiative flux estimation from the Clouds and the Earth's Radiant Energy System instrument on the *Terra* satellite. Part II: Validation, *J. Atmos. Oceanic Technol.*, in press.

Loeb, N. G., B. A. Wielicki, W. Su, K. Loukachine, W. Sun, T. Wong, K. J. Priestley, G. Matthews, W. F. Miller, and R. Davies (2006b), Multi-instrument comparison of top-of-atmosphere reflected solar radiation, *J. Clim.*, in press.

Minnis, P., D. P. Garber, D. F. Young, R. F. Arduini, and Y. Tokano (1998), Parameterizations of reflectance and effective emittance for satellite remote sensing of cloud properties, *J. Atmos. Sci.*, *55*, 3313–3339.

Minnis, P., D. F. Young, S. Sun-Mack, P. W. Heck, D. R. Doelling, and Q. Trepte (2003), CERES cloud property retrievals from imagers on TRMM, Terra, and Aqua, *Proc. SPIE Int. Soc. Opt. Eng.*, *5235*, 37–48.

Moroney, C., R. Davies, and J.-P. Muller (2002), Operational retrieval of cloud-top heights using MISR data, *IEEE Trans. Geosci. Remote Sens.*, *40*, 1541–1546.

Parol, F., et al. (2004), Capabilities of Multi-Angle Polarization Cloud measurements from satellite: POLDER results, *Adv. Space Res.*, *33*(7), 1080–1088.

Platnick, S., M. D. King, S. A. Ackerman, W. P. Menzel, B. A. Baum, C. Riedl, and R. A. Frey (2003), The MODIS cloud products: Algorithms and examples from Terra, *IEEE Trans. Geosci. Remote Sens.*, *41*, 459–473.

Remer, L. A., et al. (2005), The MODIS aerosol algorithm, products and validation, *J. Atmos. Sci.*, *62*, 947–973.

Salomonson, V. V., W. L. Barnes, P. W. Maymon, H. E. Montgomery, and H. Ostrow (1989), MODIS: Advanced facility instrument for studies of the earth as a system, *IEEE Trans. Geosci. Remote Sens.*, *27*(2), 145–153.

Smith, G. L. (1994), Effects of time response on the point spread function of a scanning radiometer, *Appl. Opt.*, *33*, 7031–7037.

Suarez, M. J. (2005), Technical report series on global modeling and data assimilation, Vol. 26: Documentation and validation of the Goddard Earth Observing System (GEOS) data assimilation system—Version 4, *NASA/TM-2005-104606*, vol. 26, 181 pp.

Suttles, J. T., B. A. Wielicki, and S. Vemury (1992), Top-of-atmosphere radiative fluxes: Validation of ERBE scanner inversion algorithm using Nimbus-7 ERB data, *J. Appl. Meteor.*, *31*, 784–796.

Wielicki, B. A., B. R. Barkstrom, E. F. Harrison, R. B. Lee III, G. L. Smith, and J. E. Cooper (1996), Clouds and the Earth's Radiant Energy System (CERES): An Earth observing system experiment, *Bull. Am. Meteorol. Soc.*, *77*, 853–868.

_____

R. Davies, Department of Physics, University of Auckland, Auckland 1142, New Zealand.

N. G. Loeb, Mail Stop 420, NASA Langley Research Center, Hampton, VA 23681-0001, USA. (n.g.loeb@larc.nasa.gov)

K. Loukachine and W. F. Miller, Science Applications International Corporation, 10260 Campus Point Drive, San Diego, CA 92121, USA.

W. Sun, Center for Atmospheric Sciences, Hampton University, Hampton, VA 23668, USA.